Received: 22 September 2021 | Revised: 30 December 2021 | Accepted: 26 January 2022

DOI: 10.1002/ctpp.202100162

ORIGINAL ARTICLE

Contributions to Plasma Physics

Modelling of electrostatic ion-scale turbulence in divertor tokamaks with the gyrokinetic code COGENT

Mikhail Dorf | **Milo Dorr**

Physics Division, Lawrence Livermore National Laboratory, Livermore, California, USA

Correspondence
Mikhail Dorf, Lawrence Livermore National Laboratory, Livermore, CA, USA.
Email: dorf1@llnl.gov

Funding information
U.S. Department of Energy, Grant/Award Number: DE-AC52-07NA27344

Abstract

Continuum gyrokinetic simulations of electrostatic ion scale turbulence are presented for the case of a diverted (single-null) tokamak geometry. The simulation model, implemented in the finite-volume code COGENT, solves the long-wavelength limit of the full-F gyrokinetic equation for ion species coupled to a vorticity equation for electrostatic potential variations, where a fluid model is used for an electron response. The model describes the ion scale ion temperature gradient (ITG) and resistive drift modes as well as neoclassical ion physics effects. Different turbulence regimes are observed depending on the plasma profiles, and the roles of a self-consistent background electric field and an X-point geometry are explored. In particular, increasing the pedestal density gradient and the corresponding radial electric field is demonstrated to suppress the ITG turbulence, whereas the same edge plasma background can still be destabilized by the resistive modes when the plasma resistivity is increased. The effects of X-point geometry are assessed by comparing cross-separatrix simulations with counterpart calculations performed for a toroidal annulus geometry. For the simulation parameters considered, similar global behaviour is observed in both cases, whereas strong local suppression of turbulence fluctuations is demonstrated near the X-point for the case of a single-null geometry.

KEYWORDS

finite-volume methods, gyrokinetics, tokamak edge

1 | INTRODUCTION

Development of *continuum* computational methods is of particular importance for full-F gyrokinetic modelling of edge plasmas, where an ion distribution function can substantially deviate from a local Maxwellian, and therefore the *particle-in-cell* (PIC) approach may require a very large number of macro-particles in order to suppress statistical noise in low-amplitude turbulence calculations subject to an adequate representation of the background quasi-equilibrium dynamics. However, complexities in the magnetic geometry of a tokamak edge, such as the presence of a magnetic separatrix, provide a challenge for efficient continuum simulations that utilize field-aligned grid structure in order to handle strong anisotropy of plasma transport. Various approaches to deal with a divertor geometry in both fluid and gyrokinetic simulations of edge plasmas have been developed over the last decade,[1–5] and recently, the first proof-of-principle 5D full-F continuum gyrokinetic simulation of ion-scale microturbulence in a single-null geometry was demonstrated with the finite-volume code COGENT.[6] The COGENT code solves the long-wavelength limit of the full-F gyrokinetic equation

for ion species coupled to a vorticity equation for electrostatic potential variations, where a fluid model is used for an electron response. The simulation model describes the ion temperature gradient (ITG) and resistive drift modes as well as neoclassical ion physics effects, and its numerical implementation utilizes a locally field-aligned multiblock coordinate system. In this discretization approach, the toroidal direction is divided into blocks, such that within each block, the grid cells are field-aligned, and a non-matching grid interface is allowed at block boundaries. The toroidal angle corresponds to the "coarse" field-aligned coordinate, whereas the poloidal cross section, comprised of the radial and poloidal directions, is finely gridded to resolve short-scale perpendicular turbulence structures and to support accurate re-mapping (interpolation) at toroidal block boundaries. Additional grid sub-blocks describing the core, scrape-off-layer (SOL) and private-flux (PF) regions are used to discretize model equations in the poloidal cross-section that spans both open and closed magnetic field-lines.

In this work, the initial cross-separatrix studies reported by Dorf and Dorr[6] are extended to provide more details about the present COGENT capabilities for edge plasma modelling. In particular, 5D simulations that now include both neoclassical (collisional) and anomalous (turbulence) transport are contrasted with the corresponding 4D (axisymmetric) simulations that only describe collisional transport. Consistent behaviour is observed during the initial transient relaxation of a local Maxwellian distribution, which is driven by the effects of finite drift–orbit width and ion–ion collisions. This result serves as an important verification of the 5D multiblock discretization algorithms and also suggests that the 4D capability can be efficiently used to study properties of the relaxed "initial" quasi-stationary state, that is, prior to its longer time-scale evolution due to turbulent and/or neoclassical transport. The analysis of transport power is performed for 4D and 5D calculations and the stiff (non-stiff) properties of turbulent (neoclassical) transport are demonstrated.

In addition, suppression of the ITG turbulence is obtained by increasing the pedestal density gradient (and thereby the corresponding radial electric field), which is consistent with the properties of H-mode. We demonstrate that the plasma stability is attributed to the effects of a self-consistent radial electric field and is not merely related to a decrease in the ITG drive, $\eta_i = L_N/L_T$, by artificially suppressing flux-surface averaged potential perturbations and observing edge destabilization. Here, $L_A^{-1} = -AdA/dr$ is the inverse logarithmic radial length scale for the background density ($A = N$) and temperature ($A = T$) variations. We further show that the ITG-stable plasma profile can be destabilized by increasing plasma resistivity and enhancing effects of the resistive drift and ballooning modes, which are driven by a pressure gradient and can play an important role in a cold plasma edge region. Finally, all aforementioned simulations are repeated for the case of a toroidal annular geometry in order to assess the influence of a magnetic X-point. For the illustrative parameters considered in this work, similar global behaviour is observed in either geometry, whereas strong local suppression of turbulence fluctuations is demonstrated near the X-point for the case of the single-null simulations.

2 | NUMERICAL MODEL

The COGENT simulation model and numerical algorithms are described in detail elsewhere,[6] and we only provide a brief summary here. The code solves the long-wavelength limit of a 5D full-F ion gyrokinetic equation written in a conservative form

$$\frac{\partial\left(B_{\parallel}^{*}f\right)}{\partial t}+\nabla\cdot\left(\dot{\mathbf{R}}B_{\parallel}^{*}f\right)+\frac{\partial}{\partial v_{\parallel}}\left(\dot{v}_{\parallel}B_{\parallel}^{*}f\right)=C\left[B_{\parallel}^{*}f_i\right]. \tag{1}$$

Here, $f\left(\mathbf{R},v_{\parallel},\mu\right)$ denotes the ion gyroaveraged distribution function, ∇ is the gradient with respect to $\mathbf{R}$ and the phase-space guiding-centre velocities are given by

$$\dot{\mathbf{R}}=\frac{1}{B_{\parallel}^{*}}\left[v_{\parallel}\mathbf{B}^{*}+\frac{c}{Z_ie}\mathbf{b}\times\left(Z_ie\nabla\Phi+\mu\nabla B\right)\right], \tag{2}$$

$$\dot{v}_{\parallel}=-\frac{1}{m_iB_{\parallel}^{*}}\mathbf{B}^{*}\cdot\left(Z_ie\nabla\Phi+\mu\nabla B\right), \tag{3}$$

where m_i and Z_i are the ion species mass and charge state, respectively, e is the electron charge, c is the speed of light, $\mathbf{B}=B\cdot\mathbf{b}$ is the magnetic field with $\mathbf{b}$ denoting the unit vector along the field, $\mathbf{B}^{*}\left(\mathbf{R},v_{\parallel}\right)\equiv\mathbf{B}+\left(cm_i/Z_ie\right)v_{\parallel}\nabla\times\mathbf{b}$,

$B_{\parallel}^{*} = \mathbf{B}^{*} \cdot \mathbf{b}$, and the long-wavelength limit, $k_{\perp}\rho_i \ll 1$, is presently adopted for electrostatic potential variations, $\Phi(\mathbf{R}, t)$, and collision models, $C\left[B_{\parallel}^{*} f_i\right]$. Here, $\rho_i = V_{Ti}/\Omega_i$ is the particle thermal gyroradius, $V_{Ti} = \sqrt{T_i/m_i}$ is the thermal velocity, $\Omega_i = Z_i eB/(m_i c)$ is the cyclotron frequency, and $k_{\perp}^{-1}$ represents the characteristic length-scale for variations in the electrostatic potential and distribution function perturbations.

Although a wide range of detailed collision models including the full nonlinear Fokker–Plank operator is available in COGENT,[7,8] for simplicity purposes, in the present work, we adopt a Lenard–Bernstein collision model[9]

$$\begin{aligned} C\left[B_{\parallel}^{*} f_i\right] &= \nu_{ii}\frac{\partial}{\partial \mathbf{v}}\left[(\mathbf{v}-\mathbf{U})B_{\parallel}^{*} f_i + \frac{T_i}{m_i}\frac{\partial B_{\parallel}^{*} f_i}{\partial \mathbf{v}}\right] \\ &= \nu_{ii}\frac{\partial}{\partial v_{\parallel}}\left[\left(v_{\parallel}-U_{\parallel}\right)B_{\parallel}^{*} f_i + \frac{T_i}{m_i}\frac{\partial B_{\parallel}^{*} f_i}{\partial v_{\parallel}}\right] + \nu_{ii}\frac{\partial}{\partial \mu}\left[2\mu B_{\parallel}^{*} f_i + 2\frac{T_i}{B}\mu\frac{\partial B_{\parallel}^{*} f_i}{\partial \mu}\right]. \end{aligned} \tag{4}$$

Here, the parallel flow velocity, $U_{\parallel}$, and the ion temperature, T_i, are defined as

$$U_{\parallel} = \frac{2\pi}{n_i m_i}\int v_{\parallel} f_i B_{\parallel}^{*} dv_{\parallel} d\mu, \tag{5}$$

$$T_i = \frac{2\pi}{3n_i}\int\left(v_{\parallel}^2 + \frac{2\mu B}{m_i}\right) f_i B_{\parallel}^{*} dv_{\parallel} d\mu, \tag{6}$$

and the ion gyrocentre density, n_i, is given by

$$n_i = \frac{2\pi}{m_i}\int f_i B_{\parallel}^{*} dv_{\parallel} d\mu. \tag{7}$$

The COGENT implementation of the collision operator in Equation (4) that discretely conserves ion momentum and energy is described in detail by Angus.[10] For simplicity purposes, in the present work, we take $\nu_{ii} = const$.

Self-consistent variations of an electrostatic potential are described by making use of the quasi-neutrality equation ($\nabla \cdot \mathbf{j} = 0$) for the vorticity variable[6]

$$\varpi = \nabla_{\perp} \cdot \left(\frac{c^2 n_i m_i}{B^2}\nabla_{\perp}\Phi\right), \tag{8}$$

$$\begin{aligned} \frac{\partial \varpi}{\partial t} + \nabla \cdot \left(c\frac{-\nabla_{\perp}\Phi \times \mathbf{b}}{B}\varpi\right) &= \nabla \cdot \left(\frac{2\pi Z_i e}{m_i}\int \mathbf{v}_{\perp}^{m} f_i B_{\parallel}^{*} dv_{\parallel} d\mu\right) + \nabla \cdot \left[\frac{cZ_i n_i T_e}{B}\left(\nabla \times \mathbf{b} + \frac{\mathbf{b} \times \nabla B}{B}\right)\right] \\ &+ B\nabla_{\parallel}\left[\frac{\sigma_{\parallel}}{B}\left(\frac{1}{eZ_i n_i}\nabla_{\parallel}\left(n_e T_e\right) - \nabla_{\parallel}\Phi + \frac{0.71}{e}\nabla_{\parallel} T_e\right)\right]. \end{aligned} \tag{9}$$

Here, $\mathbf{v}_{\perp}^{m} \equiv \dot{\mathbf{R}}_{\perp}(\Phi = 0)$ is the magnetic drift velocity corresponding to the perpendicular component of the guiding centre velocity in Equation (2) for the case of a zero potential, $\sigma_{\parallel} = 1.96 n_e e^2 \tau_e / m_e$ is the parallel electron conductivity, with τ_e denoting the basic electron collisional term given by Braginskii,[11] T_e is the electron temperature and n_e is the electron density determined from

$$n_e = \nabla_{\perp} \cdot \left(\frac{c^2 m_i n_i}{eB^2}\nabla_{\perp}\Phi\right) + Z_i n_i. \tag{10}$$

Retaining the polarization density corrections [the first term in the RHS of Equation (10)] is found to be important to provide stabilization of high-$k_{\perp}\rho_i$ perturbations. Equations (8)–(10) represent the COGENT vorticity model for self-consistent variations of the electrostatic potential that needs to be coupled with a model for an electron temperature. For simplicity purposes, here, we assume a simple isothermal response with $T_e = const$. The numerically efficient, yet physically reduced vorticity model [in Equations (8)–(10)] omits kinetic electron effects and does not include the trapped electron mode (TEM); however, it describes edge-relevant ion modes such as ITG and resistive drift and ballooning modes.

2.1 | Geometry

We make use of a model single-null geometry described in detail by Dorf and Dorr.[6] Figure 1 shows a coarse version of the flux-aligned COGENT mesh and the outer midplane radial lineout of the local magnetic safety factor, $q_{loc} = \left(B_\phi/B_\theta\right)(R - R_0)/R$, and the magnetic shear, $s_{loc} = ((R - R_0)/q_{loc})(\partial q_{loc}/\partial R)$. Here, B_ϕ and B_θ are the toroidal and poloidal components of the magnetic field, and R is the major radius coordinate with $R = R_0$ corresponding to the magnetic axis. We note that Dorf and Dorr[6] has a typo in describing the values of the magnetic safety factor. Also a wider core region is used in the present work as compared to that by Dorf and Dorr.[6] The toroidal magnetic field $I = RB_\phi = -3.5\,\mathrm{T}\cdot\mathrm{m}$ and the major radius $R_0 = 1.6\,\mathrm{m}$ are chosen to roughly correspond to those of the DIII-D tokamak.

The counterpart simulations in a toroidal annulus geometry use the same values of I and R_0 with the magnetic field specified by

$$\mathbf{B} = \frac{I}{R}\left(\frac{r}{q(r)R_0}\boldsymbol{e}_\theta + \boldsymbol{e}_\phi\right), \tag{11}$$

where (r, ϕ, θ) represents the standard toroidal coordinate system, and safety factor profile is specified by

$$q(r) = q_0 + q_1 \exp\left(q_2 \log\frac{r}{a}\right). \tag{12}$$

Here, the constants $q_0 = 1.25$, $q_1 = 3.41$, $q_2 = 2.2$ and $a = 0.687\,\mathrm{m}$ are chosen to closely match variations of the magnetic flux function of the single-null geometry at the outboard midplane [see Figure 1b].

2.2 | Boundary and initial conditions

The phase-space advection operator in the ion gyrokinetic equation [Equation (1)] requires specification of "inflow" fluxes at the phase-space boundaries. In the present studies, these fluxes are computed from the initial ion distribution. For instance, for the case of a local Maxwellian initialization, a boundary condition corresponds to the presence of a Maxwellian "bath" specified by the initial values of the density, parallel momentum and temperature at a domain boundary.

Boundary conditions for the electrostatic potential include a zero Dirichlet boundary condition on all domain boundaries except for the inner radial (core) boundary, where the following consistent boundary condition is applied:

$$\left\langle \frac{c^2 n_i m_i}{B^2}|\nabla\psi|^2 \right\rangle \frac{\partial \Phi}{\partial \psi} = \int_0^t dt \left\langle \nabla\psi \cdot \mathbf{j}_i \right\rangle. \tag{13}$$

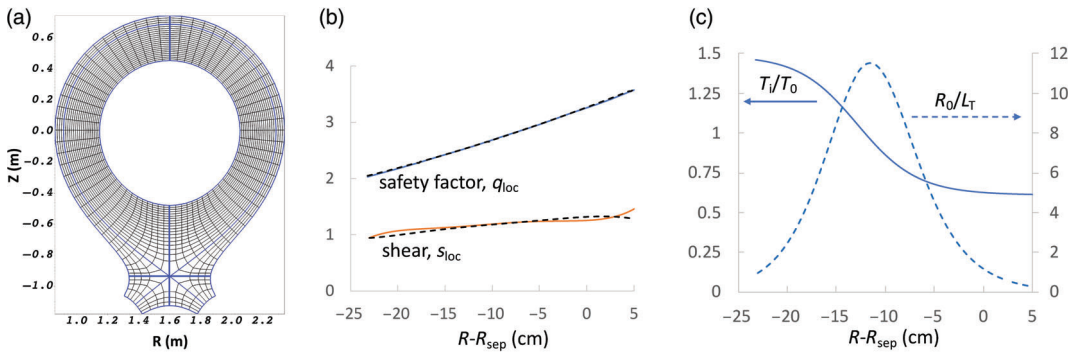

FIGURE 1 Simulation geometry and initial conditions. (a) A coarse version of the flux-aligned mesh in the poloidal plane. The poloidal block boundaries are illustrated with the bold blue curves. (b) Outer midplane radial lineout of the local safety factor q_{loc} (blue curve) and local magnetic shear s_{loc} (orange curve). The corresponding values of q_{loc} and s_{loc} for the toroidal annular geometry are illustrated with the black dashed lines. (c) Outer midplane radial lineout of the initial normalized ion temperature, T_i/T_0, and inverse radial scale length, $R_0/L_T = -(R_0/T_i)\,\partial T_i/\partial R$ determined from Equation (15) with $T_{out} = 0.6T_0$, $T_{in} = 1.5T_0$, $\psi_{mid} = 0.8$, $\Delta\psi_N = 0.1$

Here, $\mathbf{j}_i = (2\pi Z_i e/m_i) \int \dot{\mathbf{R}} f_i B_\parallel^* dv_\parallel d\mu$ is the ion gyrocentre current density and $\langle \chi \rangle$ is the flux-surface average defined as the volume average of χ between two neighbouring flux surfaces, ψ and $\psi + d\psi$. The condition in Equation (13) makes use of the quasi-neutrality equation, where a small contribution from the flux surface average of the radial electron current is neglected, and the potential, Φ, is assumed to be nearly constant on the boundary flux surface.[6] Such a condition allows for consistent development of the long-wavelength background radial electric field at the radial boundaries, while plausibly mitigating near-boundary turbulence by suppressing short-wavelength poloidal variations in Φ. The use of the boundary condition in Equation (13) can accommodate large plasma gradients at the radial boundaries as demonstrated in Section 3. This alleviates the need for radial buffer regions, which are typically included in continuum full-F gyrokinetic simulations that employ the standard, that is, Dirichlet or Neumann, conditions and use the buffer zones to diffuse the profile gradients and damp the turbulence.[12–14]

The ion distribution function is initialized with an unshifted local Maxwellian distribution

$$F_M = N(\psi_N) \left(\frac{m_i}{2\pi T(\psi_N)} \right)^{3/2} \exp\left(-\frac{m_i v_\parallel^2}{2T(\psi_N)} - \frac{\mu B}{T(\psi_N)} \right), \tag{14}$$

where the plasma density, $N(\psi_N)$, and temperature, $T(\psi_N)$, profiles are given by

$$A(\psi_N) = A_{out} + \frac{A_{in} - A_{out}}{2} \left[1 - \tanh\left(\frac{\psi_N - \psi_{mid}}{\Delta\psi_N} \right) \right]. \tag{15}$$

Here, ψ_N is the normalized magnetic flux function, which corresponds to zero at the magnetic axis and to unity at the last closed flux surface (LCFS). The initial value of an electrostatic potential is set to zero, $\Phi(t = 0) = 0$.

3 | SIMULATION RESULTS

In this section, we present numerical results from several illustrative COGENT simulations to demonstrate the present code capabilities for the modelling of edge plasmas in single-null geometries. Figures 2 and 3 demonstrate the results of a 5D simulation that includes both neoclassical and turbulence-driven transport. The simulation is initialized with a uniform density profile, $N = N_0$ and a temperature profile specified by Equation (15) with $T_{out} = 0.6T_0$, $T_{in} = 1.5T_0$, $\psi_{mid} = 0.8$, $\Delta\psi_N = 0.1$ and $T_0 = 4.0\,\text{keV}$ [see Figure 1c]. Single-charged, $Z_i = 1$, deuterium ions, $m_i = 2m_p$ are considered with the characteristic ion gyro-radius corresponding to $\rho_i = 0.4\,\text{cm}$, where $\rho_i = V_{T0}/\Omega_i$, $V_{T0} = \sqrt{T_0/m_i}$ and $\Omega_i = (Z_i e/m_i)(|I|/R_0)$. The electron temperature is taken to be consistent with the characteristic ion temperature, $T_e = T_0$. The collision frequency in the ion–ion collision model [see Equation (4)] is taken as uniform with $\nu_{ii} = 0.01 V_{T0}/\left(\overline{q} R_0\right)$, and we also consider a uniform parallel conductivity $\sigma_\parallel = 1.96 n_e e^2 \overline{\tau}_e / m_e$ corresponding to $\overline{\tau}_e \omega_{tr,e} = 0.6$. Here, $\omega_{tr,e} = V_{T_e}/\left(\overline{q} R_0\right)$, $V_{T_e} = \sqrt{T_e/m_e}$, and we take $\overline{q} = 2.5$. A periodic toroidal wedge with $\Delta\phi = 2\pi/8$ is considered, and a single toroidal block is used. Note that the fundamental toroidal mode, $n = 8$, corresponds to $k_\theta \rho_i = n\overline{q}\rho_i/a = 0.012$ for the case of field-aligned turbulence, and therefore, the considered toroidal domain width is sufficient to capture most of the ion-scale turbulence spectrum. The grid resolution in the poloidal plane is specified by $\left[N_\psi = 76,\ N_\theta = 512\right]$, $\left[N_\psi = 16,\ N_\theta = 576\right]$, and $\left[N_\psi = 16,\ N_\theta = 64\right]$, in the core, SOL and PF regions, respectively, where N_α denotes the number of grid points in the direction α. The number of cells in the other phase-space directions is $\left[N_\phi = 4, N_{v\parallel} = 32,\ N_\mu = 24\right]$, and the velocity space extent is given by $-4.9 V_{T0} \le 4.9 V_{T0}$ and $0 \le \mu \le 10.9 T_0 R_0/|I|$.

Figure 2 demonstrates the time evolution of the electrostatic potential and the radial transport power and particle flow defined as

$$Q = \frac{1}{Q_N} \oint dA_\psi \int \frac{2\pi}{m_i} B_\parallel^* dv_\parallel d\mu \left(\frac{m_i v_\parallel^2}{2} + \mu B + Z_i e\Phi \right) \left(\dot{\mathbf{R}} \cdot \boldsymbol{e}_\psi \right) f_i, \tag{16}$$

$$\Gamma = \frac{1}{\Gamma_N} \oint dA_\psi \int \frac{2\pi}{m_i} B_\parallel^* dv_\parallel d\mu \left(\dot{\mathbf{R}} \cdot \boldsymbol{e}_\psi \right) f_i. \tag{17}$$

Here, $Q_N = \left(\rho_i^2/L_T^2\right) N_0 T_0 V_{T0} S$ and $\Gamma_N = \left(\rho_i^2/L_T^2\right) N_0 V_{T0} S$ are normalization factors, $L_T = 33\,\text{cm}$ is the characteristic value of the length scale for temperature variations, $S = 36\,\text{m}^2$ is the tokamak surface area corresponding to $R_{sep} - R = 13\,\text{cm}$ and $\boldsymbol{e}_\psi$ and dA_ψ are the normal unit vector and a face area element of a magnetic flux surface, respectively. The

surface integrals in Equations (16) and (17) are computed over the entire toroidal surface; therefore the flux integrals measured over the $\Delta\phi$ wedge in our 5D simulations are then multiplied by the $2\pi/\Delta\phi$ factor to obtain the corresponding diagnostic values. The results in Figures 2 and 3 show that the simulation begins with a transient stage, $0 \le t \lesssim 20R_0/V_{T0}$, during which the initial local Maxwellian distribution relaxes towards a quasi-stationary state. Strong geodesic acoustic mode (GAM) excitation occurs during the relaxation stage, where the observed GAM frequency is consistent with its theoretical estimate[15,16]

$$\omega_{GAM}^2 \approx \left(\frac{7}{4}+\chi\right)\frac{2T_i}{m_i R_0^2}\left[1+\frac{46+32\chi+8\chi^2}{(7+4\chi)^2 q^2}\right]. \tag{18}$$

Taking $\chi \equiv Z_i T_e/T_i = 1$, $q = \bar{q} = 2.5$ and $T_i = T_0$ we obtain $\omega_{GAM} \approx 2.5V_{T0}/R_0$. Note that although a nearly adiabatic electron response corresponds to a negligible flux surface averaged radial electron current on closed flux surfaces, a pronounced ion particle flow exists during the initial not-intrinsically ambipolar transient dynamics as can be seen from Figure 2a. This particle flow, however, nearly vanishes as the system reaches the quasi-stationary intrinsically ambipolar state (as described in detail by Hirshman.[17]). Following the relaxation to the quasi-stationary state, the ion-scale instability develops [see Figure 3b], which results in a burst of transport power around $t = 26R_0/V_{T0}$. Finally, the developed microturbulence stage is observed for $t \gtrsim 40R_0/V_{T0}$. The potential perturbations during that stage are shown in Figure 3c,d, demonstrating the field-aligned nature of the microturbulence.

To elucidate the role of neoclassical and turbulent transport, the 5D simulations illustrated in Figures 2 and 3 are repeated with the 4D full-F axisymmetric version of the code that does not include the effects of microturbulence.

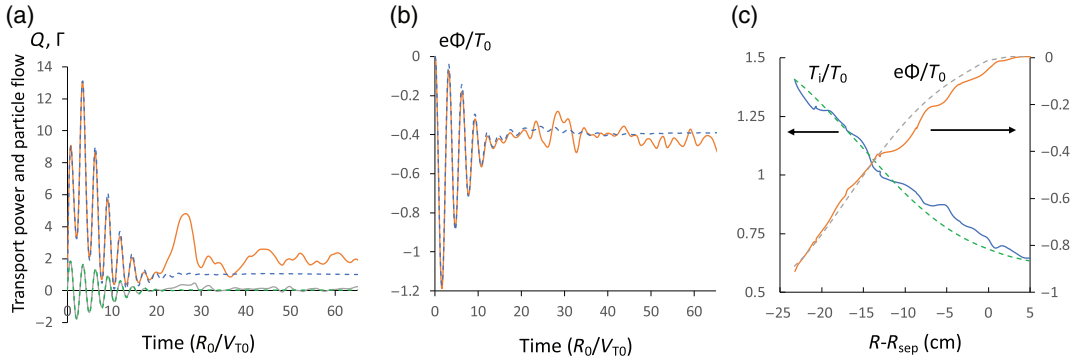

FIGURE 2 Full-F simulations of ion transport in a single-null geometry. (a) Time history of the radial transport power and particle flow measured in the 5D simulation (shown by the solid orange and grey curves, respectively) and in the 4D simulations (shown by the dashed blue and green curves, respectively). (b) Time history of the potential perturbations measured in the 5D (solid orange curve) and 4D (dashed blue curve) simulations. (c) Outer midplane radial lineout of the potential and ion temperature variations obtained in the 5D (solid curves) and 4D (dashed curves) simulations. The time histories in Frames (a) and (b) are measured at the outer midplane coordinate $R_{sep} - R = 13$ cm, and the radial profiles in Frame (c) are measured at the time instance $t = 59.7R_0/V_{T0}$

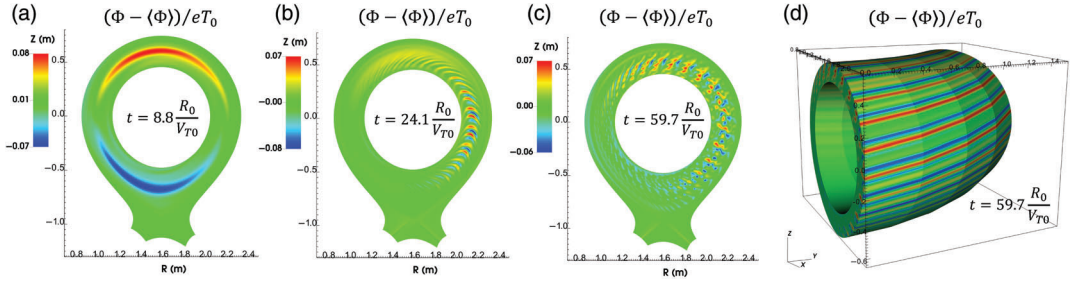

FIGURE 3 Non-zonal component of potential variations, $\widetilde{\Phi} = (\Phi - \langle\Phi\rangle)/eT_0$, corresponding to (a) initial nearly-axisymmetric relaxation, (b) unstable mode development and (c) ion-scale microturbulence. Frame (d) illustrates the field-aligned structure of the developed microturbulence

Such neoclassical simulations can be performed with a coarser grid resolution, for which we adopt $[N_\psi = 38,\ \ N_\theta = 64]$, $[N_\psi = 8,\ \ N_\theta = 72]$ and $[N_\psi = 8,\ \ N_\theta = 8]$, in the core, SOL and PF regions, respectively. All other parameters are the same as in the corresponding 5D simulations. Comparing the 5D and 4D results in Figure 2a,b, we observe consistent evolution of the system parameters during the initial transient stage. This result serves as an important verification of the 5D multiblock discretization algorithms and also suggests that the 4D capability can be efficiently used to study properties of the relaxed "initial" quasi-stationary state, that is, prior to its longer time-scale evolution due to turbulent and/or neoclassical transport.

We further analyse properties of neoclassical and turbulent transport by lowering the boundary condition for the ion temperature at the inner radial (core) boundary from $T_{in} = 1.5T_0$ to $T_{in} = 1.2T_0$ and observing the corresponding change in the transport power that is required to support different temperature profiles. For these studies, we turn off ion–ion collisions in the 5D simulations in order to study properties of turbulence-driven transport in the absence of collisional damping. The radial profiles of the ion temperature and the transport power are shown in Figures 4 and 5 for the 4D and 5D simulations, respectively. Note that the transport power plots also illustrate the "offset" values, Q_{offset}, that are measured by making use of the diagnostics in Equation (16) for the case of collisionless 4D simulations, where no heat transport is expected. We note that the transport power diagnostic yields vanishing values of collisionless Q in the axisymmetric local limit, which assumes an ion orbit width to be much smaller than the length scale for ion temperature variations. Therefore, the offset values shown in Figures 4c and 5c are associated with non-local effects of the ion drift orbit motion (c.f. diamagnetic heat fluxes due to Larmor orbit motion). Analysing the 4D results in Figure 4, we find that the decrease of the collisional transport power, $Q - Q_{\text{offset}}$, associated with the decrease in the temperature boundary value, is consistent with the local theoretical estimate for neoclassical transport, $Q_{NC} \propto TdT/d\psi$ for $\nu_{ii} = const$. Namely, the ratio of $Q(\psi) - Q_{\text{offset}}(\psi)$ measured for $T_{in} = 1.2T_0$ and $T_{in} = 1.5T_0$, $\{Q(\psi) - Q_{\text{offset}}(\psi)\}_{T_{in}=1.2T_0} / \{Q(\psi) - Q_{\text{offset}}(\psi)\}_{T_{in}=1.5T_0}$, is found to agree with the corresponding ratio of $\{T(\psi)dT/d\psi\}_{T_{in}=1.2T_0}/\{T(\psi)dT/d\psi\}_{T_{in}=1.5T_0}$ within 10% accuracy, which, however, can be attributed to the nonlocal effects. Non-axisymmetric 5D simulations demonstrate much stiffer transport properties. Indeed, comparing Figures 4 and 5, it follows that the difference in the length scale for temperature variations is smaller in the core region $20\text{cm} \lesssim (R_{sep} - R) \lesssim 5\,\text{cm}$ of the 5D simulations (where the turbulence is most developed) as compared to the core region of the counterpart 4D neoclassical simulations. At the same time, the increase in the transport power, $Q - Q_{\text{offset}}$, required to transition between $T_{in} = 1.2T_0$ and $T_{in} = 1.5T_0$ cases is larger for the 5D simulations.

Our next studies explore the role of a self-consistent background radial electric field, E_r, and plasma resistivity. For these purposes, we repeat the simulations reported in Figures 2 and 3 by increasing the value of the plasma conductivity 10 times $(\overline{\tau}_e\omega_{tr,e} = 6.0)$ in order to suppress the role of the resistive drift and ballooning modes. The potential perturbations of the ITG-dominated turbulence are shown in Figure 6a. We then introduce a density gradient in the initial plasma distribution specified by Equation (15) with $N_{out} = 0.6N_0$, $N_{in} = 1.5N_0$, $\psi_{mid} = 0.8$, $\Delta\psi_N = 0.2$ [see Figure 7a], and repeat the previous simulation. The complete mitigation of the ITG instability is observed [see Figure 6b] and the stabilizing role of self-consistent axisymmetric E_r [see Figure 7b] is elucidated by repeating the simulation in Figure 6b for the case where the flux surface averaged (zonal) component, $\langle\Phi\rangle$, is artificially suppressed by subtracting it from the total potential, Φ, after each time step. In the absence of a large background radial electric field and the corresponding $E \times B$ flow shear

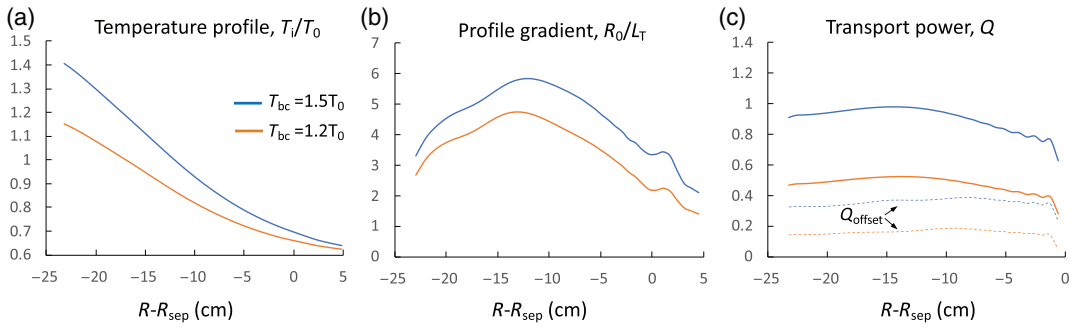

FIGURE 4 Results of the 4D collisional simulations illustrating neoclassical transport properties for $T_{bc} = T_{in} = 1.5T_0$ (blue curves) and $T_{bc} = T_{in} = 1.2T_0$ (orange curves) values of the ion temperature core boundary condition. The data in Frames (a)–(c) correspond to the time instance $t = 91R_0/V_{T0}$. The dashed curves in Frame (c) illustrate the time-averaged "offset" values of transport power measured in the 4D collisionless simulations within the $61R_0/V_{T0} \le t \le 91R_0/V_{T0}$ time interval

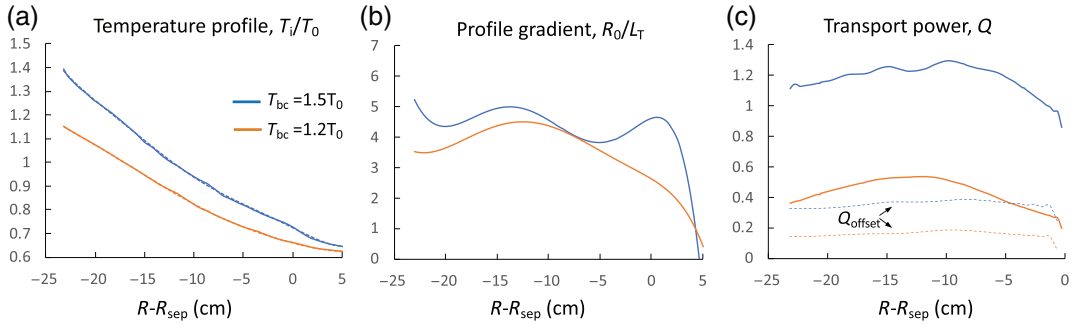

FIGURE 5 Results of the 5D collisionless simulations illustrating anomalous (turbulence-driven) transport properties for $T_{bc} = T_{in} = 1.5T_0$ (blue curves) and $T_{bc} = T_{in} = 1.2T_0$ (orange curves) values of the ion temperature core boundary condition. The data in Frames (a) and (c) correspond to time averages over the $61R_0/V_{T0} \leq t \leq 91R_0/V_{T0}$ time interval. The dashed curves in Frame (a) correspond to sixth-order polynomial fitted data, which is used to compute the temperature profile gradient illustrated in Frame (b). The dashed curves in Frame (c) illustrate the time-averaged "offset" values of transport power measured in the 4D collisionless simulations

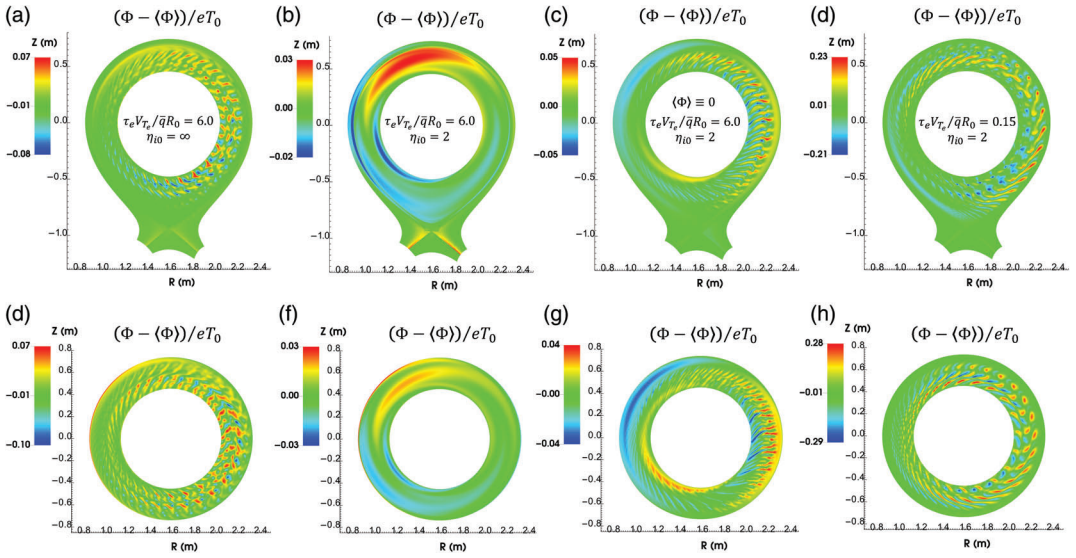

FIGURE 6 Effects of a radial electric field, plasma resistivity and X-point geometry on the electrostatic ion-scale turbulence. The non-zonal component of potential variations, $\widetilde{\Phi} = (\Phi - \langle\Phi\rangle)/eT_0$, is shown for the cases corresponding to (a) ITG-dominated turbulence, (b) ITG-stable background plasma profiles, (c) re-occurrence of the ITG turbulence [for the plasma profiles from Frame (b)] induced by suppressing the zonal-component of the electrostatic potential $\langle\Phi\rangle$ and (d) resistive-modes dominated turbulence [for the plasma profiles from Frame (b)]. The results in Frames (e)–(h) correspond to the counterpart simulations performed in the toroidal annulus geometry. Notice local suppression of the turbulence perturbations near the X-point region by comparing Frames (a) and (d) with Frames (e) and (h), respectively

the microturbulence reoccurs as seen in Figure 6c. Next, we decrease the value of the plasma conductivity by a factor of 40 $\left(\overline{\tau}_e\omega_{tr,e} = 0.15\right)$ and again repeat the ITG-stabilized simulation illustrated in Figure 6b. The decrease in conductivity significantly enhances the role of the resistive modes driven by the pressure gradient [see Figure 7c], and as a result, we observe the presence of strong resistive turbulence with cross-separatrix blob-like activity as shown in Figure 6d.

Finally, we address the role of the X-point geometry by repeating the simulations illustrated in Figure 6a–d for the case of the toroidal annulus geometry described in Section 2.2. The corresponding results are illustrated in Figure 6e–h. The initial temperature and density profiles for the annulus case are chosen to be consistent with the counterpart single-null simulations. Similar global behaviour is observed in either geometry, whereas strong local suppression of turbulence fluctuations is demonstrated near the X-point for the case of the single-null simulations. Additional details of the simulations in the two geometries are illustrated in Figure 7. In particular, Figure 7b shows the outboard lineout plots of the

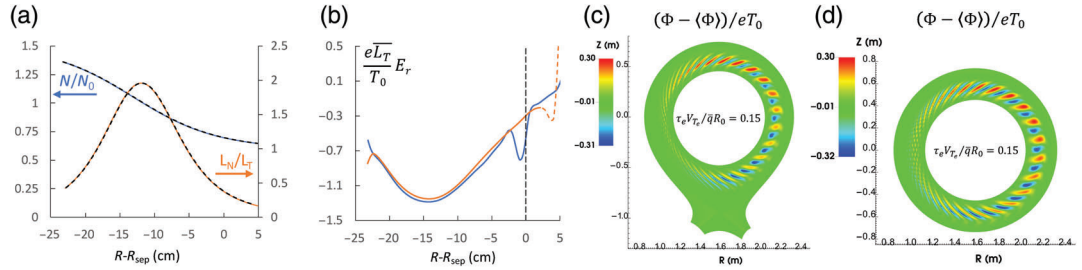

FIGURE 7 Comparison of simulation results obtained for the X-point and toroidal annulus geometries. (a) Outer midplane radial lineout of the initial density profile, N_i/N_0, (blue curve) and $\eta_i = L_N/L_T$ (orange curve) for the case of the X-point geometry. The corresponding values of N_i/N_0 and η_i for the toroidal annular geometry are illustrated with the black dashed lines. (b) Outer midplane radial lineout of the normalized radial electric field, $e\overline{L_T}E_r/T_0$, for the X-point (blue curve) and annulus (orange curve) geometries obtained at $t = 38.7R_0/V_{T0}$. The dashed part of the orange curve highlights an artefact of a near-boundary numerical solution for the case of the annulus geometry, which however is not found to significantly affect the global results. Frames (c) and (d) demonstrate the dominant resistive mode corresponding to the high-resistivity case, $\tau_e V_{T_e}/\bar{q}R_0 = 0.15$, for the X-point and annulus geometries, respectively

normalized background radial electric field, $e\overline{L_T}E_r/T_0$, obtained in the simulations with stabilized turbulence shown in Figure 6b,f for the X-point and the toroidal annulus geometry, respectively. Here, $\overline{L_T} = R_0/11.5$ is the minimal value of the logarithmic radial length scale for the initial ion temperature variations. While the radial electric field profiles appear to be similar between the two geometries, the X-point geometry case is distinguished by a near-separatrix E_r-well attributed to ion orbit loss. A modest size of the E_r-well-well observed in the present studies is related to a rather large density value [see the initial density profile in Figure 7a] used for a Maxwellian bath boundary condition at the divertor plates, which provides substantial inflow of ions and thereby compensates for the orbit loss effect. Assessing the influence of the ion orbit loss driven $E \times B$ shear on cross-separatrix turbulence, for example, by varying the ion inflow from the plates, will be the subject of our future studies.

4 | CONCLUSIONS

A locally field-aligned multiblock version of the 5D full-F finite-volume code COGENT has been developed to perform gyrokinetic plasma simulations in single-null geometries. A distinguishing feature of the underlying numerical algorithm is the use of multiple toroidal blocks, such that within each block the grid cells are field-aligned and a non-matching (non-conformal) grid interface is allowed at block boundaries. The multiblock approach together with the use of the toroidal angle as a field-aligned coordinate can minimize the twist and shear of the field-line following cells and can facilitate numerical simulations of plasma microturbulence in a divertor (single-null) geometry. The physical model captures the effects of neoclassical transport and electrostatic ion scale microturbulence including the ITG and resistive drift and ballooning modes. In this work, we present results from illustrative COGENT simulations performed for the case of a model single-null geometry that demonstrates the present code capabilities and lay a groundwork for numerical modelling of the existing tokamak facilities and critical edge-plasma processes such as L-H transition. In particular, the role of neoclassical and turbulence transport is addressed by making use of the 4D (axisymmetric) and 5D (non-axisymmetric) code versions. The stabilizing effects of a self-consistent radial electric field are demonstrated by contrasting 5D simulations that include a self-consistent axisymmetric component of potential perturbations, $\langle\Phi\rangle$, with simulations that artificially suppress $\langle\Phi\rangle$. The effects of resistive drift and ballooning modes are addressed by varying plasma conductivity and observing significant resistive microturbulence with cross-separatrix blob-like features in cases where the ITG turbulence is stabilized. Finally, local stabilizing effects of the magnetic X-point are demonstrated by comparing single-null simulations with the counterpart calculations performed for the case of a toroidal annulus geometry.

ACKNOWLEDGMENTS

The authors are grateful to D. Ghosh and M. Umansky for fruitful discussions. This research was supported by the U.S. Department of Energy under contract DE-AC52-07NA27344.

DATA AVAILABILITY STATEMENT

The data that support the findings of this study are available from the corresponding author upon reasonable request.

REFERENCES

[1] F. Hariri, M. Ottaviani, *Comput Phys Commun* **2013**, *184*, 2419.
[2] M. Giacomin, P. Ricci, *J Plasma Phys* **2020**, *86*(5), 905860502.
[3] A. Stegmeir, A. Ross, T. Body, M. Francisquez, W. Zholobenko, D. Coster, O. Maj, P. Manz, F. Jenko, B. N. Rogers, K. S. Kang, *Phys Plasmas* **2019**, *26*(5), 052517.
[4] M. R. Dorr, P. Colella, M. A. Dorf, D. Ghosh, J. A. F. Hittinger, P. O. Schwartz, *J Comput Phys* **2018**, *373*, 605.
[5] M. Dorf, M. Dorr, *Contrib Plasma Phys* **2018**, *58*, 434.
[6] M. Dorf, M. Dorr, *Phys Plasmas* **2021**, *28*(3), 032508.
[7] M. A. Dorf, R. H. Cohen, M. Dorr, T. Rognlien, J. Hittinger, J. Compton, P. Colella, D. Martin, P. McCorquodale, *Phys Plasmas* **2013**, *20*(1), 012513.
[8] M. A. Dorf, R. H. Cohen, M. Dorr, J. Hittinger, T. D. Rognlien, *Contrib Plasma Phys* **2014**, *54*, 517.
[9] A. Lenard, I. B. Bernstein, *Phys Rev* **1958**, *112*, 1456.
[10] J. R. Angus, *Ph.D. Thesis*, University of California, San Diego, **2012**.
[11] S. I. Braginskii, *Rev Plasma Phys* **1965**, *1*, 205.
[12] Y. Idomura, *Phys Plasmas* **2014**, *21*(2), 022517.
[13] V. Grandgirard, J. Abiteboul, J. Bigot, T. Cartier-Michaud, N. Crouseilles, G. Dif-Pradalier, C. Ehrlacher, D. Esteve, X. Garbet, P. Ghendrih, G. Latu, M. Mehrenberger, C. Norscini, C. Passeron, F. Rozar, Y. Sarazin, E. Sonnendrücker, A. Strugarek, D. Zarzoso, *Comput Phys Commun* **2016**, *207*, 35.
[14] Y. Asahi, V. Grandgirard, Y. Idomura, X. Garbet, G. Latu, Y. Sarazin, G. Dif-Pradalier, P. Donnel, C. Ehrlacher, *Phys Plasmas* **2017**, *24*(10), 102515.
[15] M. A. Dorf, R. H. Cohen, M. Dorr, T. Rognlien, J. Hittinger, J. Compton, P. Colella, D. Martin, P. McCorquodale, *Nucl Fusion* **2013**, *53*(6), 063015.
[16] Z. Gao, K. Itoh, H. Sanuki, J. Q. Dong, *Phys Plasmas* **2008**, *15*(7), 072511.
[17] S. P. Hirshman, *Nucl Fusion* **1978**, *18*(7), 917.

How to cite this article: M. Dorf, M. Dorr, *Contributions to Plasma Physics* **2022**, e202100162. https://doi.org/10.1002/ctpp.202100162